Journal of Materials Chemistry A

ROYAL SOCIETY OF CHEMISTRY

REVIEW

View Article Online
View Journal | View Issue

Cite this: J. Mater. Chem. A, 2025, 13, 17261

Probing solid-state battery aging: evaluating calendar *vs.* cycle aging protocols *via* time-resolved electrochemical impedance spectroscopy†

Thao Kim Truong, [a] Grace Whang,[a] Jake Huang,[a] Stephanie Elizabeth Sandoval[a] and Wolfgang G. Zeier *[ab]

Understanding battery aging mechanisms is critical towards identifying and improving upon performance bottlenecks. Aging protocols which can quickly identify and monitor degradation of cells can help expedite solid-state battery development by predicting the possible long-term aging trend of cells in a time efficient manner. In this work, the degradation behavior of In/InLi|Li_6PS_5Cl|NCM83:Li_6PS_5Cl cells was investigated using two different accelerated aging protocols: (1) calendar aging and (2) cycle aging. Cells with various cut-off potentials were investigated using the two aging protocols showing significantly greater performance deterioration under calendar aging relative to cycle aging. Applying distribution of relaxation times analyses obtained from impedance spectroscopy, the cathode–electrolyte interfacial resistance evolution is found to be the dominant degradation mechanism during calendar aging while changes at the anode–electrolyte interface are influential during cycle aging tests. The aging protocol and analyses applied in this work can potentially be further extended to other systems to help understand degradation processes and quickly screen cells for optimization.

Received 10th February 2025
Accepted 12th May 2025

DOI: 10.1039/d5ta01083g

rsc.li/materials-a

Introduction

Solid-state batteries (SSBs) have emerged as one of the key battery developments in moving towards high energy density batteries in both the academic and commercial research space. While traditional lithium-ion batteries (LIBs) with liquid electrolytes are backed by decades of research and development, SSBs have only more recently experienced a rebirth in research efforts since the report of $Li_{10}GeP_2S_{12}$ having ionic conductivities on par with their liquid electrolyte counterparts.[1] Having high energy density and potentially improved safety, SSBs containing lithium metal or silicon anodes are considered highly promising for the next generation of secondary batteries.[2,3] While much progress has been made in the recent years, commercialization of SSBs still faces the hurdle of ensuring both safety and performance.[4] Focusing on the latter, improving SSB electrochemical performance towards their commercialization is an ongoing challenge. Degradation at the cathode active material–solid electrolyte interface and formation of an interphase consisting of decomposition products is one of the key challenges inhibiting cell performance.[5,6] In addition, batteries will gradually age over the course of cycling, leading to the drop of their performance, which is intimately correlated with interphase formation.[7,8] Currently, various factors have been reported to influence degradation (aging) processes in LIBs such as charging mode, operating temperature, or state of charge (SoC).[9,10] Therefore, it is important to develop methods to both efficiently and rapidly screen cell materials and improve understanding of the aging processes.

Battery aging is generally categorized into calendar aging and cycle aging.[9] Because of the meta-stable nature of electrochemical processes within the cells, battery aging occurs not only during operation but also at rest. Under long-term storage, cells undergo continuous degradation that reduces usable capacity which is referred to as calendar aging.[7] In contrast, cycle aging refers to battery performance deterioration stemming from repeated cycling.[10] This aging should also depend on the current density employed. Both types of aging are important to understand, as they can involve different mechanisms and produce different effects. While cell aging studies have been well established for LIBs, they are far less developed for their SSB counterparts.[11] Conventional real time battery calendar aging studies typically include alternating periods of open circuit voltage (OCV) and reference performance tests (RPTs) to evaluate cell degradation.[7] This approach requires month-long to year-long periods to sufficiently evaluate time-dependent

[a]Institute of Inorganic and Analytical Chemistry, University of Münster, 48149 Münster, Germany. E-mail: wzeier@uni-muenster.de

[b]Institute of Energy Materials and Devices (IMD), IMD-4: Helmholtz-Institut Münster, Forschungszentrum Jülich, 48149 Münster, Germany

† Electronic supplementary information (ESI) available: Li_6PS_5Cl synthesis, cathode composite preparation, cell assembly procedure, Nyquist and Bode plots during aging steps, galvanostatic charge–discharge data during accelerated calendar aging periods. See DOI: https://doi.org/10.1039/d5ta01083g

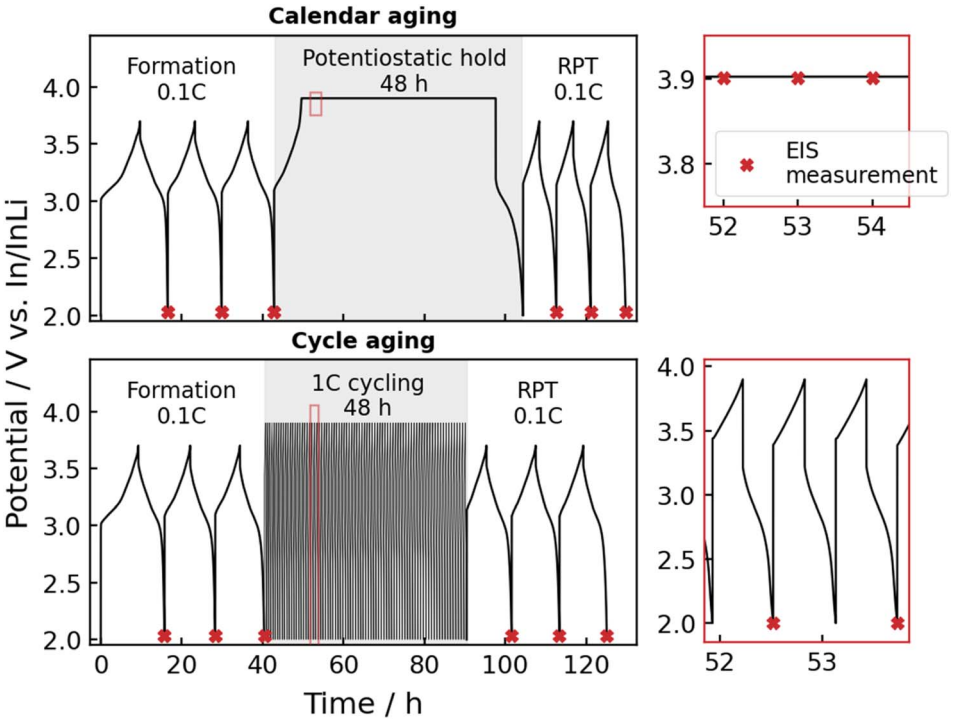

Fig. 1 Example of cell potential profiles during accelerated aging protocols. Formation and reference performance test (RPT) steps are fixed in all experiments with a variation of upper cut-off potential in aging periods (grey field). Cross mark (✕) symbols represent points where EIS measurement was recorded. An EIS measurement was implemented every hour during potentiostatic hold and end of discharge of every two cycles during 1C cycling. For formation and RPT steps, EIS was measured at the end of discharge for every cycle.

aging with the majority of time spent at OCV, which can be extremely resource-intensive when screening numerous active material and electrolyte combinations. In this regard, the design and application of fast screening protocols[10,12] can help expedite SSB development and innovation by predicting the long-term aging of batteries in a fraction of the time. This is especially important as the number of different solid electrolyte classes and components is increasing continuously. Thus far, only a few studies have looked into investigating interfacial degradation in SSBs using calendar aging protocols,[5,13–15] which used rest periods at OCV or held a specific potential for 20–30 hours with electrochemical impedance spectra (EIS) measured periodically. However, short-term OCV and voltage hold phases may provide limited information on cell degradation due to significant reversible lithiation/delithiation relaxation.[7] Diagnostic measurements for cells at the same SoC are also needed for comparison after an aging period. The need for studies on calendar and cycle aging has been shown before,[16,17] however, a comprehensive comparison of different aging approaches is still missing.

In this work, accelerated calendar and cycle aging protocols are introduced to SSBs based on $LiNi_{0.83}Co_{0.11}Mn_{0.06}O_2$ (NCM83) cathode active material (CAM) to evaluate their efficacy for probing and identifying degradation processes electrochemically. The cell configuration In/InLi|Li_6PS_5Cl|NCM:Li_6PS_5Cl, which has been thoroughly studied with known degradation mechanisms,[8,15,18] was employed as a well-characterized system against which to test these electrochemical methods. A potentiostatic hold (also known as float test or voltage hold) protocol[3,6] was employed as a qualitative accelerated tool for calendar aging tests, while a high C-rate (1C) cycling approach[19] was used for cycle aging experiments (see Fig. 1). The aging period, which was conducted in between the formation and reference performance test (RPT) steps, was fixed at 48 hours, while the upper cut-off potential is varied. Through time-resolved EIS measurements, cathode–electrolyte interfacial resistance evolution was found to be the dominant degradation mechanism during calendar aging, while changes to the anode–solid electrolyte interface were the most influential during cycle aging experiments. The results suggest that the employed potentiostatic hold (calendar aging) protocol may be a better means than high C-rate cycling (cycle aging) to probe and predict cell degradation. The work presented here shows that aging experiments coupled with various electrochemical characterization and analytical techniques such as EIS, differential capacity (dQ/dV), and distribution of relaxation times (DRT) allow for the interpretation and deconvolution of physicochemical processes within the cell during and after aging. With the employed aging protocols, the findings of this work on degradation at the electrode–electrolyte interface provide another perspective in understanding SSB degradation.

Results and discussion

Accelerated aging tests were performed for In/InLi|Li_6PS_5Cl|NCM83:Li_6PS_5Cl cells at various upper cut-off potentials of

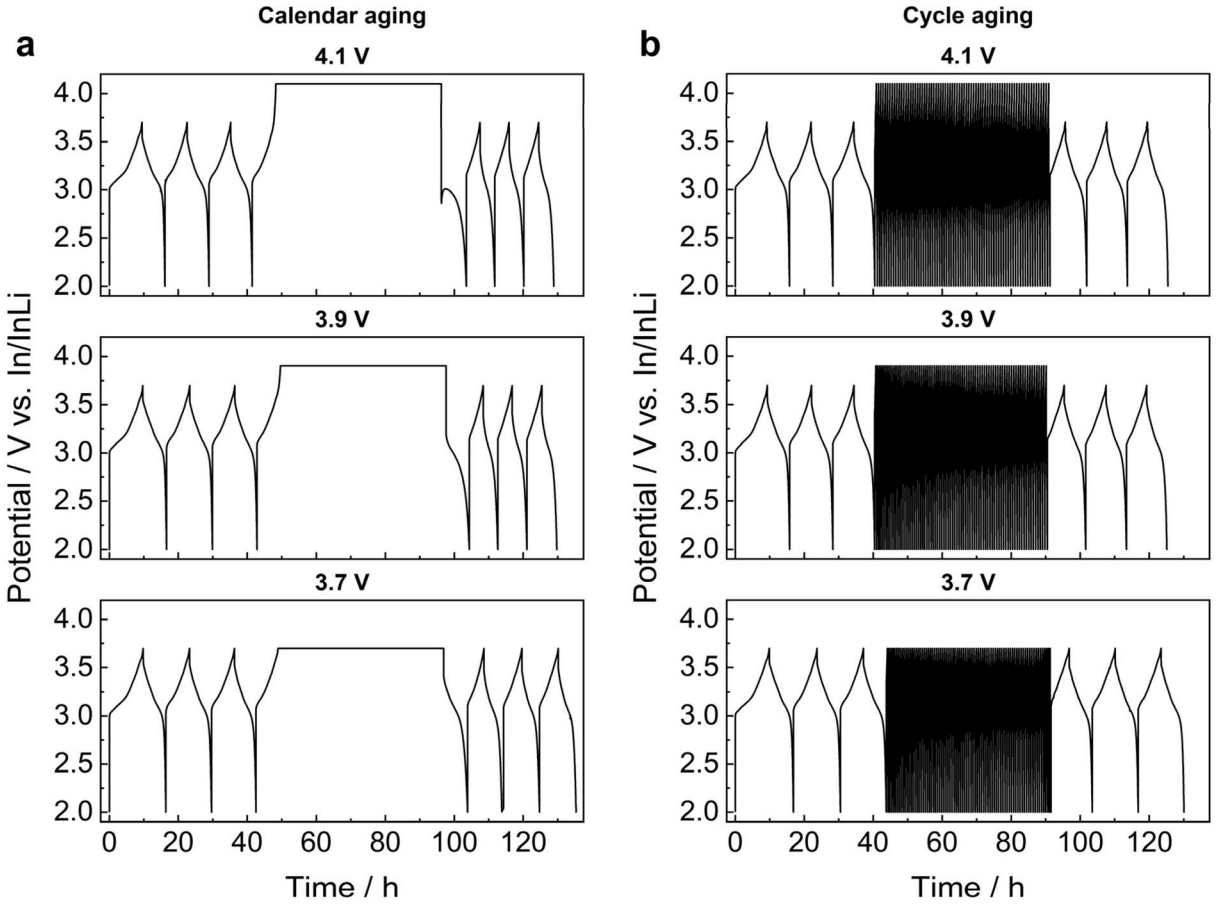

Fig. 2 Potential *versus* time profile of accelerated (a) calendar aging and (b) cycle aging cells at different cut-offs. Data from all investigated cut-offs can be found in Fig. S1.†

3.7 V, 3.8 V, 3.9 V, 4.0 V, and 4.1 V *vs.* In/InLi, which correspond to 4.32 V, 4.42 V, 4.52 V, 4.62, and 4.72 V *vs.* Li^+/Li, respectively. These high potentials were selected because typical degradation of sulfide solid electrolytes (SEs) against NCM is triggered when CAM potential exceeds 3.58–3.7 V *vs.* In/InLi.[5,13,15] Results from the selected cut-off potentials of 3.7 V, 3.9 V, and 4.1 V *vs.* In/InLi are presented in the main text for brevity and visual clarity. The data from all investigated cut-off potentials for the following figures can be found in the ESI.†

Potential *versus* time profiles in Fig. 2 provide the first information on the impact of accelerated aging protocols on cell performance. For all calendar aged cells (Fig. 2a), two observations were made: (1) a significant decrease in post-aging cycle time was observed across all cells whereby increasing cut-off potentials resulted in decreasing post-aging cycle times. (2) For calendar aged cells with a 4.1 V potentiostatic hold cycle, during the first discharge step after the potentiostatic hold, a kink is observed in the galvanostatic curve (Fig. 2a, top). This may originate from lithiation processes of decomposition products, leading to severe post-aging capacity loss as shown in Fig. 3a. In contrast, for cycle aged cells (Fig. 2b), differences between the pre-aging and post-aging charge–discharge times were minor.

The formation step in batteries typically consist of a series of low-rate cycles to create an initial stable solid electrolyte interphase layer, which can stabilize the cell from further fast interfacial degradation.[20,21] Therefore, in both aging protocols, a formation step is included prior to applying a potential static hold or high current cycling. Thus, to compare cell performance before and after aging tests, the last (3^{rd}) formation cycle in this study was chosen to represent the nominal pristine cell conditions, while the final (3^{rd}) RPT cycle was chosen to represent cell conditions after accelerated aging. This should mitigate most effects of potential residual reactions after the aging period. Data for the formation and RPT cycles are shown in Fig. S1–S4 and S5,† respectively. As presented in Fig. 3a and b, calendar aged cells exhibit greater capacity fading after 48 hours of potentiostatic hold, while cycle aged cells show little capacity loss after 48 hours of high-current cycling. As the cut-off potential is increased, cells from calendar aging protocols show a trend of increasing capacity loss. The slight excess discharge capacity ($Q_{discharge} > Q_{charge}$) in the last RPT cycles as shown in Fig. 3a is likely due to continuous side reactions or residual reversible capacity gained from potentiostatic hold.

Correlated differential capacity (dQ/dV) plots (Fig. 3c and d) of charge–discharge curves can reveal more information about cell redox behavior with phase transitions during cell cycling.[22]

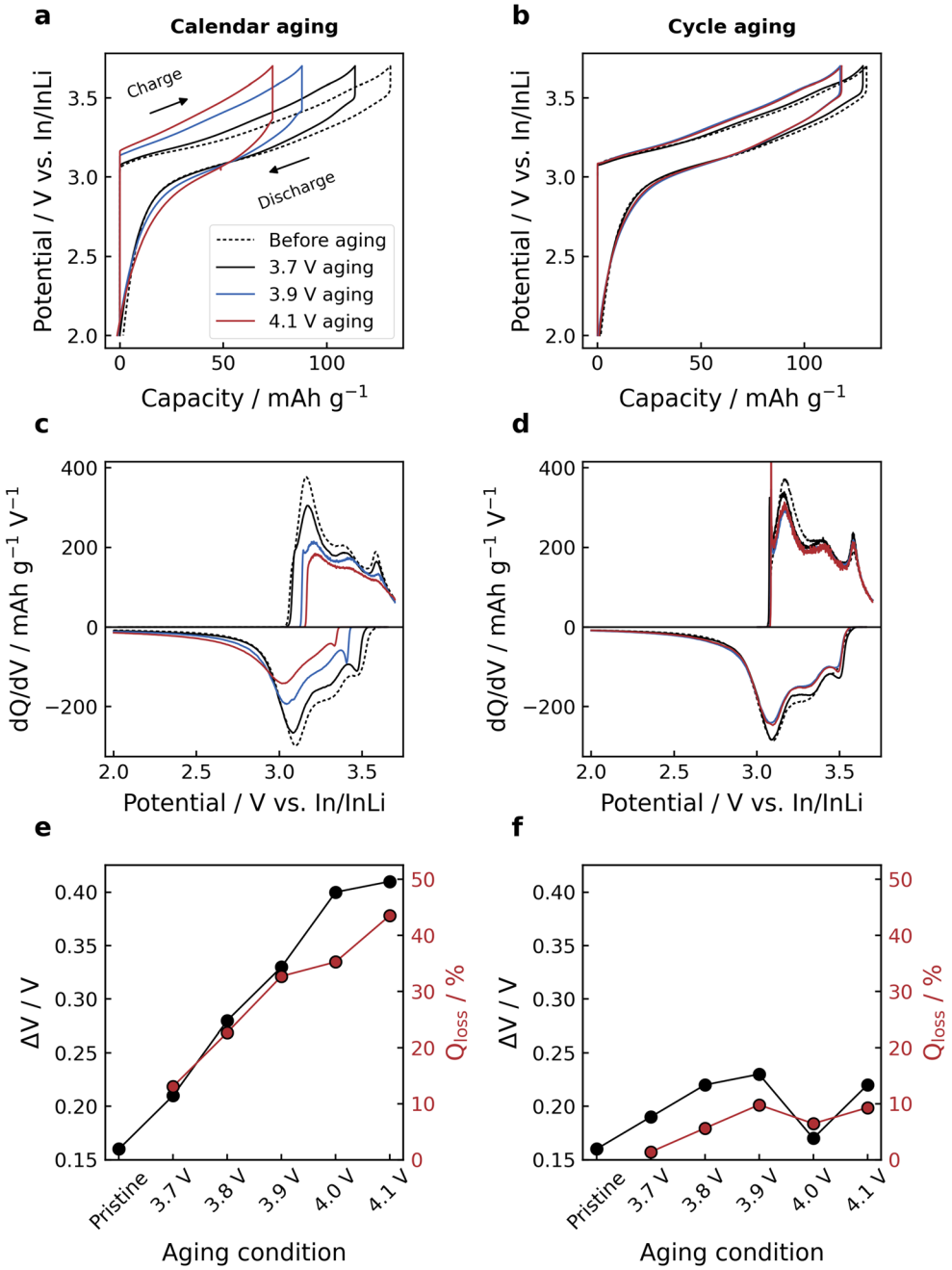

Fig. 3 Data measured in the last formation cycles (before aging) and last RPT cycles (aging). (a and b) Potential *versus* capacity profiles, (c and d) corresponding differential capacity plots, and (e and f) comparison of voltage gap and capacity loss of accelerated calendar and cycle aging cells, respectively. Data from all investigated cut-offs can be found in Fig. S2.†

Substantial detrimental effects of accelerated aging protocols are observed for calendar aged cells, which show a significant decrease in dQ/dV peak intensity post-aging. This suggests the loss of lithium inventory in the CAM[23] due to parasitic processes during the voltage hold. Additionally, the increase in peak-to-peak separation of the reductive and oxidative processes with increasing cut-off potential suggests that exposure of the cell to higher voltages not only further expedite degradation but also lead to increased polarization. With cycle aged cells, only small changes in dQ/dV peak positions and only a slight decrease in peak intensity were observed.

The voltage difference between the charge and discharge curves are commonly referred to as the voltage hysteresis and directly influence the energy efficiency of the battery.[24] To better compare the impact of accelerated aging protocols on cell performance, the voltage difference (ΔV) of the charge–discharge curves as well as the percentage of capacity loss (Q_{loss}) were estimated from the data of Fig. 3a and b. ΔV was calculated at 50% SoC to avoid the non-linear behaviors at very low or high

SoC. The percentage of capacity loss before and after accelerated aging was calculated using:

$$Q_{\text{loss}} = 1 - \frac{Q_{\text{last RPT discharge}}}{Q_{\text{last formation discharge}}} \quad (1)$$

As shown in Fig. 3e and f, both calendar and cycle aged cells exhibit a correlation between ΔV and capacity loss. Calendar aged cells exhibit a strong increase in ΔV and Q_{loss} with increasing cut-off potential. Cycle aged cells show a similar, but much less severe, trend up to 3.9 V, but degradation appears to plateau at higher voltages. Following the preliminary results, the utility and limitations of the aging protocols used in this work will be further discussed below.

(Electro)chemical decomposition at the sulfide SE-CAM interface producing a resistive interphase layer has been reported experimentally as one of the most critical factors causing overpotential increases and deteriorating cell performance in SSB.[5,25] While sulfide SEs exhibit excellent ionic conductivity and deformability compared to other types of SEs, their narrow electrochemical window and poor chemical compatibility with electrode materials remain a significant challenge, limiting their potential for future applications.[26] Zuo *et al.* reported that at the Li_6PS_5Cl-NCM85 and $Li_{5.5}PS_{4.5}Cl_{1.5}$-NCM85 interfaces, electrochemical decomposition of Li_6PS_5Cl and $Li_{5.5}PS_{4.5}Cl_{1.5}$ took place as the cells were operated at voltages as low as 3.58 V *vs.* In/InLi.[15] Furthermore, at cut-off potential from 3.58 V *vs.* In/InLi, interphase formation can be a combination between SE and CAM consumption processes, which could also produce oxygenated decomposition species such as sulfites/sulfates, phosphates, O_2 and SO_2.[7] Similar phenomena were observed for the $Li_{5.5}PS_{4.5}Cl_{1.5}$-NCM83 interface by Hartel *et al.*, where strong interfacial degradation was triggered in the In/InLi|$Li_{5.5}PS_{4.5}Cl_{1.5}$|NCM83:$Li_{5.5}PS_{4.5}Cl_{1.5}$ half-cells when the cathode potential exceeded 3.7 V *vs.* In/InLi,[11] leading to electrochemical decomposition of the SE and chemical degradation of the NCM. In addition to the cathode–electrolyte interphase formation, it was reported that the increased cathode–electrolyte interfacial resistance may also be contributed by the contact loss between them.[27] Here, we use time-resolved EIS measurements and DRT analysis to examine the interfacial degradation in the aged cells electrochemically.

To better understand the interfacial resistance evolution of the tested cells, EIS data were collected before, during, and after the aging periods (points where EIS measurement was recorded are illustrated in Fig. 1). While EIS is a rich information source, the deconvolution of physical processes from Nyquist plots *via* equivalent circuit models can be highly ambiguous due to overlapping response frequency ranges.[28] Therefore, the fitting of impedance data was implemented using DRT analysis, which does not require an *a priori* established model of discrete impedance contributions.[29] Typical DRT results are illustrated in Fig. 4, while further details on the calculation method by Huang *et al.*[30] can be found in the ESI.† Peaks in the DRT in specific time constant ranges are typically interpreted to represent electrochemical processes within the cell. As the time constant τ is defined as $\tau = RC$, the observed time constants of different processes reflect both their resistances and characteristic capacitances. Conduction processes, such as bulk or grain boundary ionic conduction, are generally fast, with small capacitances and very short relaxation times. However, reactions at the electrode–electrolyte interface such as interfacial charge transfer exhibit substantially larger capacitances, resulting in longer relaxation times.[31] The DRT in this work generally indicates five main peaks, which are denoted as P_{SE}, P_{C1}, P_{C2}, P_A, and P_D in order of ascending time constant. Appearing at the shortest time constant ($\tau \sim 10^{-8}$ s), P_{SE} represents bulk resistance of the SE (R_{SE}),[31,32] which relates to ionic transport in Li_6PS_5Cl. Since Li_6PS_5Cl is a fast ion conductor, Li-ion transport relaxes at higher frequencies than the maximum measured frequency, such that the Nyquist semicircle and corresponding DRT peak are truncated. Two overlapping peaks P_{C1} ($\tau \sim 10^{-3}$ to 10^{-2}) and P_{C2} ($\tau \sim 10^{-2}$ to 10^{-1} s) can be ascribed to Li-ion transport through the cathode–electrolyte interface (R_{C1}) and interfacial charge transfer resistance (R_{C2}) within the cathode composite, respectively.[31,33] It should be noted that although a single DRT peak typically represents a physicochemical process, processes with similar time constants may cause significant peak overlap and inhibit individual peak resolution. Since P_{C1} and P_{C2} overlap strongly in almost all experiments, we refer to their combination simply as the P_C region. P_A ($\tau \sim 10^{-1}$ to 1 s) can be attributed to the charge-transfer resistance at the anode–electrolyte interface (R_A).[31,34] Lastly, P_D ($\tau \sim 10$ s) exhibits the highest time constant and

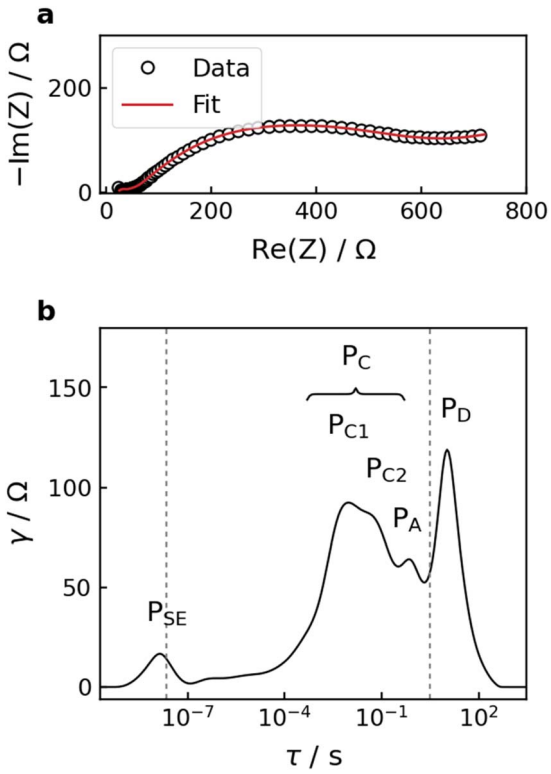

Fig. 4 (a) Typical Nyquist plot with DRT fit and (b) respective DRT analysis of the impedance data. The dashed lines in the DRT mark the high- and low-frequency boundaries of the measured range in EIS.

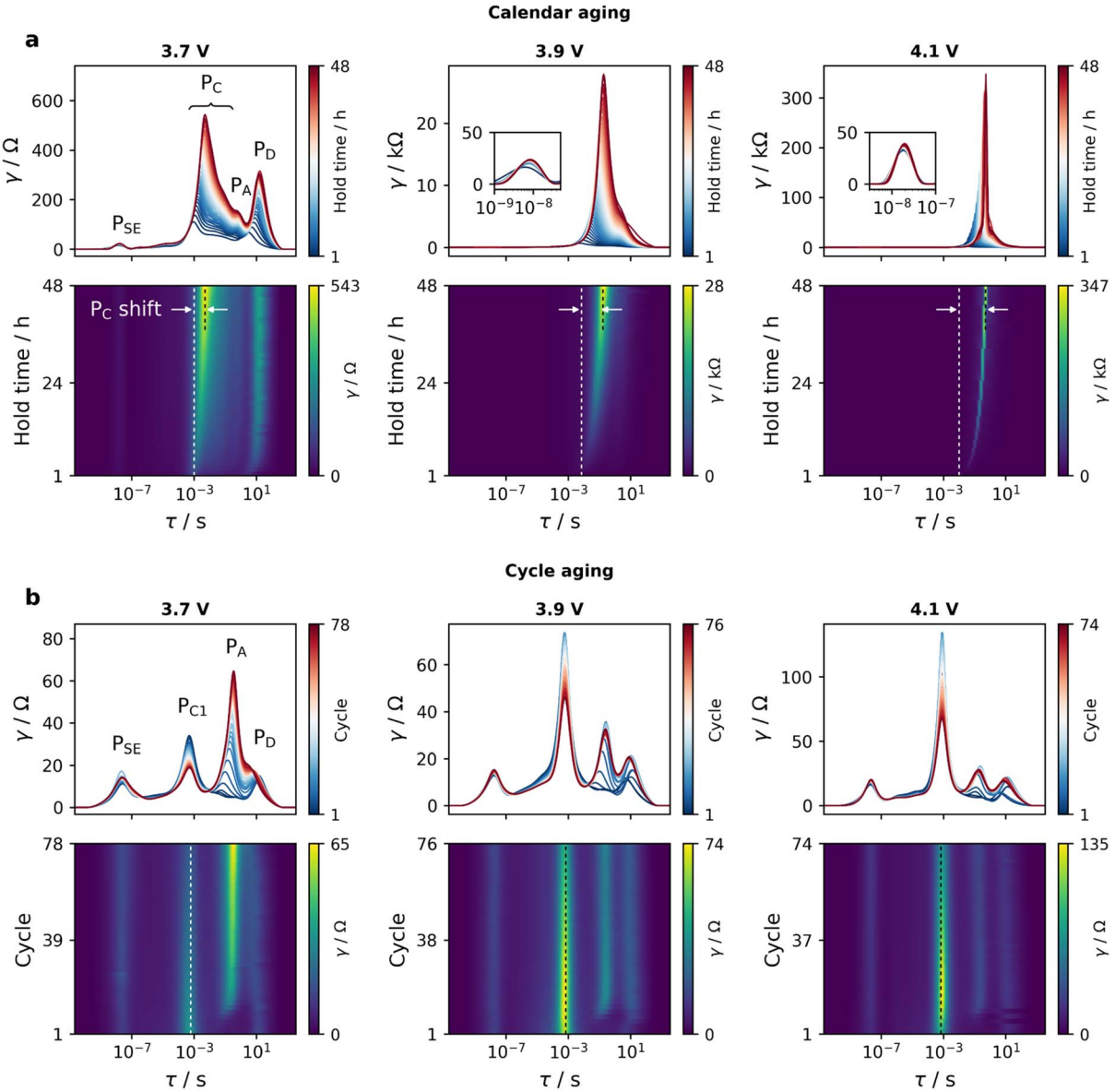

Fig. 5 DRT evolution and corresponding 2D DRT surfaces (a) during potentiostatic hold and (b) at end of discharge of cycles in high C-rate regime. In 2D DRT, the maximum value displayed on each color bar represents approximately the highest DRT intensity and the dashed lines indicate the relative position of P_C peak. Data from all investigated cut-offs with Nyquist and Bode plots can be found in Fig. S6–S9.†

represents the solid-state lithium diffusion process within the cathode electrode.[34] However, it is important to point out that the relaxation of P_{SE} and P_D occurs largely out of the measured frequency range, which correspond to the high-frequency truncated semicircle and low-frequency Warburg-like tail in Nyquist plots, respectively. Thus, P_{SE} can be referred to as a lumped high-frequency resistance contribution, which is the sum of the ohmic resistance and the truncated R_{SE}.

As can be seen in one-dimensional (1D) DRT data in Fig. 5, the changes in R_{SE} magnitude are insignificant throughout all the experiments, indicating that accelerated aging stages do not cause severe bulk degradation of the Li_6PS_5Cl SE. During the potentiostatic hold (Fig. 5a), the evolution of the DRT is dominated by the P_C region. The dominance of P_C becomes stronger with increasing cut-off potentials. In contrast, cells subjected to high C-rate cycling (Fig. 5b) exhibit fast growth of P_A in the early stages. This could be attributed to the non-uniform local current density distribution at the interface with the In/InLi alloy electrode at high current density, which may lead to inhomogeneous lithiation/delithiation processes[32] and induce chemo-mechanical degradation such as contact loss or void formation at the anode–electrolyte interface.[35,36]

Compared to the dramatic growth of the P_C region during potentiostatic holds, cathode–electrolyte interfacial processes are relatively stable in the high C-rate regime, remaining at much lower magnitudes. This suggests that more detrimental effects occur at the Li_6PS_5Cl-NCM83 interface during

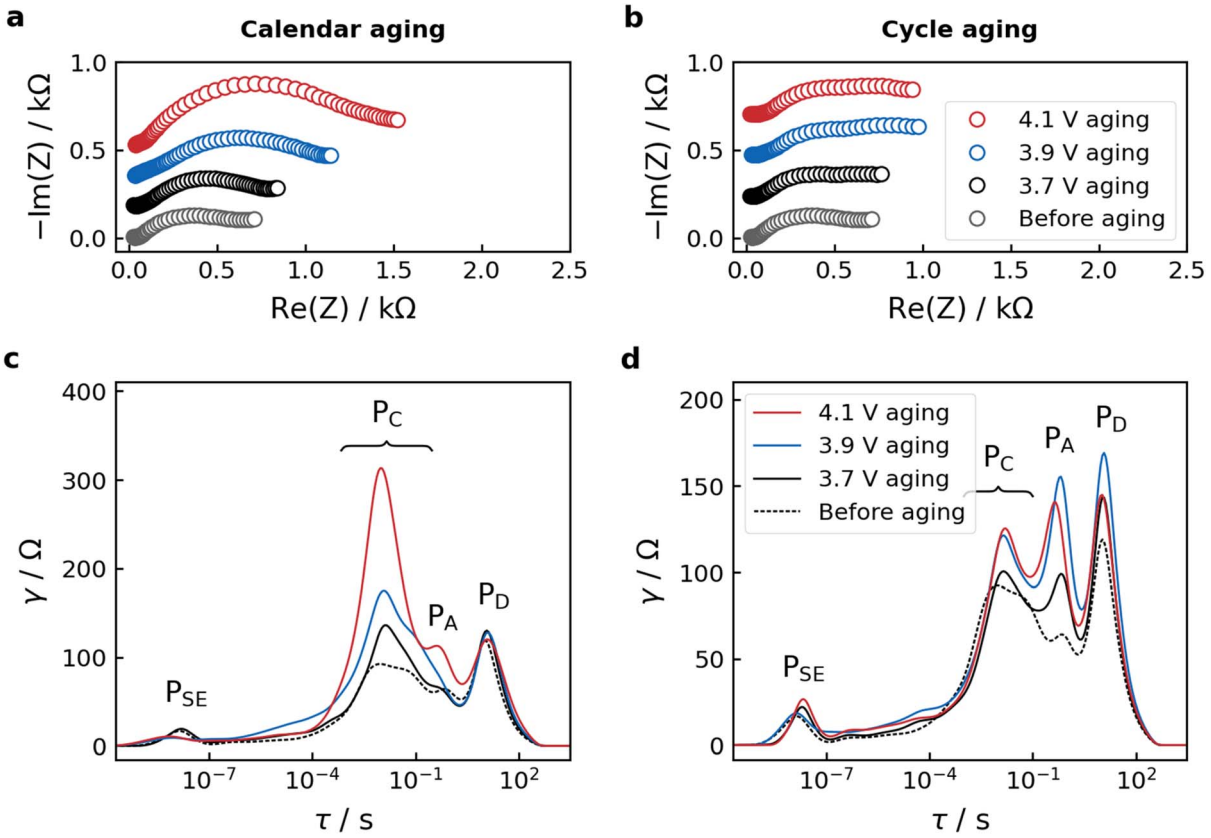

Fig. 6 Data measured at the last formation cycles (before aging) and last RPT cycles (aging). (a and b) Nyquist plots and (c and d) DRT of calendar and cycle aging cells, respectively. Data from all investigated cut-offs can be found in Fig. S10.†

potentiostatic hold, increasing interfacial resistance and inhibiting effective interfacial transfer of lithium ions.

Although the 1D DRT obtained by fitting individual impedance measurements can help deconvolute frequency-overlapped processes, peak resolution remains challenging as there are always some processes that are strongly obscured or dominant. To mitigate this, 1D DRT data can be aggregated to form two-dimensional (2D) DRT surfaces that extend along the aging time dimension to gain another view of aging mode influences on the DRT evolution. While peak shift can be observed to some extent with 1D DRT, it can be seen more clearly with 2D DRT. As displayed in Fig. 5a, the dominance of the P_C region during calendar aging in 1D DRT is also exhibited in 2D DRT, in which P_C tends to shift to longer time constants as the potentiostatic hold time increases. This may be caused by an increase in the R_{C2}/R_{C1} ratio, or a simple increase of R_{C1} while the corresponding capacitance value of P_{C1} remains almost constant. As the cut-off potential increases, larger P_C peak shifts are observed. During cycle aging (Fig. 5b), only P_A shifts to longer timescales at the beginning of the aging period.

To better compare cells, EIS measurements were also conducted at the end of discharge of formation and RPT cycles, as displayed in Fig. 6a and b. As anticipated, compared to pre-aging cell (before aging), calendar aged cells (Fig. 6c) show a noticeable domination of P_C that increases gradually with increasing cut-off potential, while P_A has a smaller contribution to the overall impedance. The combination of impedance data and DRT analyses here suggests that post-aging capacity fading in calendar aged cells (Fig. 3a) may be caused by irreversible loss of cyclable lithium into building up resistive cathode–electrolyte interphase layer as a result of parasitic side reactions. Calendar aging period may also cause chemomechanical degradation of the composite cathode such as cracking or contact loss due to volume expansion from overcharging. In contrast, cycle aged cells (Fig. 6d) only show a slight increase in the overall post-aging impedance. Again, a larger contribution from P_A is observed in these cells.

In calendar aging tests, the capacity obtained during the voltage hold can comprise of contributions from reversible and irreversible processes. At the beginning of the potentiostatic hold regime, the measured capacity can be dominated by residual reversible processes due to depolarization effect as the current decreases. Until the cell equilibrates gradually to a constant potential, irreversible processes should begin to dominate and reflect the cell's calendar aging behaviors with irreversible capacity contribution, which could be ascribed to lithium inventory consumption into forming decomposition products.[7] In a critical study on different LIB systems, Schulze *et al.* reported that the potentiostatic hold method is incapable of quantitatively forecasting the actual rate of capacity fade, but can be applied as a qualitative method for fast screening of cell systems with promising electrode–electrolyte combination.[7]

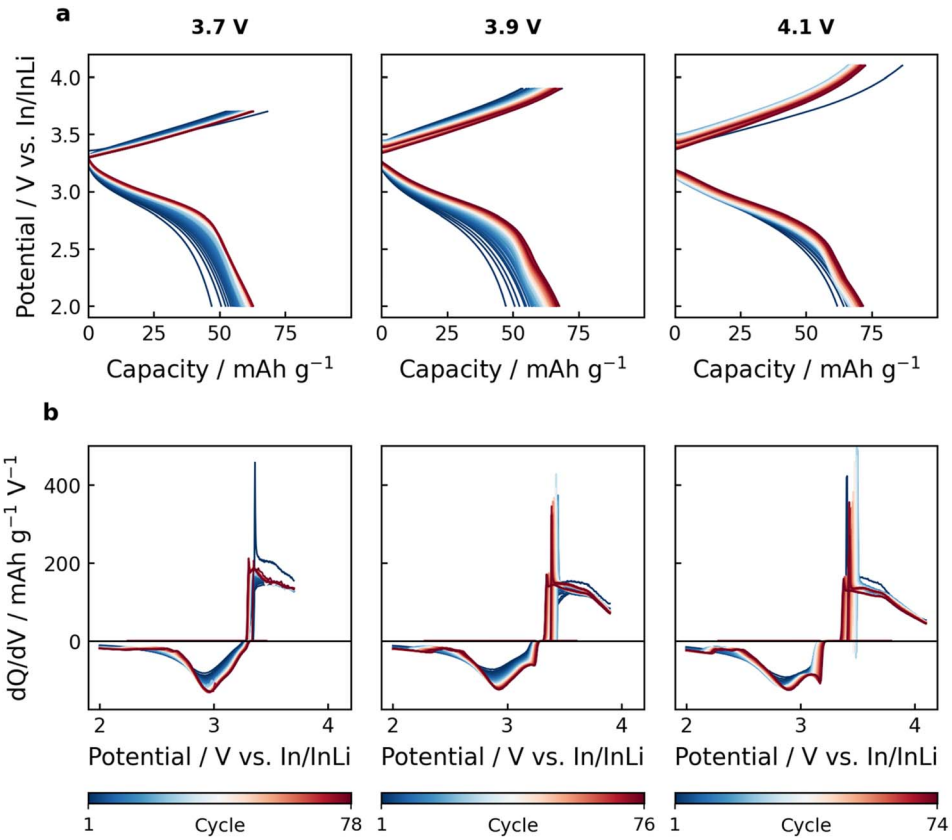

Fig. 7 (a) Galvanostatic charge–discharge curves and (b) corresponding differential capacity plots during accelerated cycle aging (1C cycling) periods. Data from accelerated calendar aging periods and all investigated cut-offs can be found in Fig. S12–S14.†

Therefore, the growth trends of capacity obtained during potentiostatic hold at different cut-off potentials may not be necessarily correlated with the capacity loss. While the growth trends of measured capacity and currents during potentiostatic hold (Fig. S11†) and post-aging capacity loss (Fig. 3e) show some correlation, the contribution of irreversible capacity loss due to parasitic reactions remains ambiguous and is yet to be quantitatively deconvoluted. Thus, an attempt to fit and extrapolate potentiostatic hold data using classical time dependency models employed in literature[5,37] may yield inaccurate results.

Although cell performance is slightly affected by high-current mode during the cycle aging period, the employed cycle aging protocol does not fully capture the expected cell aging behavior driven by interfacial degradation. In 48 hours of aging, the reduced time spent at unfavorable upper cut-off potentials during high C-rate cycling likely explains its less detrimental impact compared to potentiostatic holds. However, the galvanostatic charge–discharge data from 1C cycling periods (Fig. 7a) still provide insight into cycling behavior. The low capacity delivered during 1C cycling may be primarily attributed to kinetic limitations at high C-rate regimes. In these conditions, the CAM may not have enough time to fully undergo all the phase transitions. Additionally, the speed of the electrochemical reactions and associated transport processes cannot keep up with the demands for fast charging–discharging. The dQ/dV peak intensity decreases drastically in 1C regimes (Fig. 7b) compared to that in 0.1C (Fig. 3d), reflecting a significantly reduced capacity realization. The slight increase in capacity and dQ/dV peak intensity during cycle aging may be explained by the decline of R_{C1} over time (Fig. 5b). Moreover, high current rates may further expedite inhomogeneous reactions, resulting in broader intercalation-related dQ/dV peaks[22] with far more increases in the peak-to-peak separation of the reductive and oxidative processes.

Long-term cycling data from comparable SSB cell systems have shown that cathode–electrolyte interfacial resistance evolution is one of the main factors contributing to capacity fading.[13,15] This is in good agreement with the results of accelerated calendar aging tests in this work, suggesting the feasibility of this method for fast cell screening. Whereas the high-current cycling approach is mainly inhibited by kinetic limitations, the employed potentiostatic hold method may enable quicker screening of SSB cell chemistries by providing qualitative insights on cell degradation. To validate and improve SSB systems, future research should focus on further developing coordinated and fast prognostic techniques to diagnose aging effects in SSBs. In practice, the cut-off potential is a very important factor in attaining a balance between effective capacity and cell lifetime. Thus, depending on the cell chemistry, modifications to the testing protocols (*e.g.*, cut-off potential, potentiostatic hold time) may be applied to quickly

determine the effective cut-off potential that ensures good capacity while optimizing lifetime of the battery cell.

Conclusions

In this work, In/InLi|Li_6PS_5Cl|NCM83:Li_6PS_5Cl solid-state cell aging mechanisms were investigated by means of accelerated calendar and cycle aging protocols. From the combination of EIS and DRT analyses, cathode–electrolyte interfacial resistance evolution is found to be the dominant degradation mechanism during the calendar aging tests, while increasing charge-transfer resistance at the anode–electrolyte interface is an influencing factor during cycle aging tests. With significant cell performance deterioration after calendar aging tests, differential capacity analyses revealed the useful aspects of the employed potentiostatic hold protocol, which is recommended over the high C-rate cycling approach to qualitatively inspect and screen promising new solid-state cell chemistries in a fraction of time. It is expected that this work could contribute to the optimization of solid-state battery chemistries and charging protocols, with a focus on improving electrode–electrolyte compatibility in the pursuit of long-lasting solid-state batteries.

Data availability

After publication, the underlying data of this work will be available on the research data repository of the University of Münster at **https://doi.org/10.17879/14908422666**.

Conflicts of interest

The authors declare no conflicts.

Acknowledgements

The authors acknowledge financial support from ProRec project funded by the Bundesministerium für Bildung und Forschung (BMBF, project 03XP0537A).

References

1 N. Kamaya, K. Homma, Y. Yamakawa, M. Hirayama, R. Kanno, M. Yonemura, T. Kamiyama, Y. Kato, S. Hama, K. Kawamoto and A. Mitsui, *Nat. Mater.*, 2011, **10**, 682–686.
2 T. Krauskopf, F. H. Richter, W. G. Zeier and J. Janek, *Chem. Rev.*, 2020, **120**, 7745–7794.
3 D. H. S. Tan, Y.-T. Chen, H. Yang, W. Bao, B. Sreenarayanan, J.-M. Doux, W. Li, B. Lu, S.-Y. Ham, B. Sayahpour, J. Scharf, E. A. Wu, G. Deysher, H. E. Han, H. J. Hah, H. Jeong, J. B. Lee, Z. Chen and Y. S. Meng, *Science*, 2021, **373**, 1494–1499.
4 J. Janek and W. G. Zeier, *Nat. Energy*, 2023, **8**, 230–240.
5 T. T. Zuo, R. Rueß, R. Pan, F. Walther, M. Rohnke, S. Hori, R. Kanno, D. Schröder and J. Janek, *Nat. Commun.*, 2021, **12**, 6669.
6 T. Famprikis, P. Canepa, J. A. Dawson, M. S. Islam and C. Masquelier, *Nat. Mater.*, 2019, **18**, 1278–1291.
7 M. C. Schulze, M.-T. F. Rodrigues, J. D. McBrayer, D. P. Abraham, C. A. Apblett, I. Bloom, Z. Chen, A. M. Colclasure, A. R. Dunlop, C. Fang, K. L. Harrison, G. Liu, S. D. Minteer, N. R. Neale, D. Robertson, A. P. Tornheim, S. E. Trask, G. M. Veith, A. Verma, Z. Yang and C. Johnson, *J. Electrochem. Soc.*, 2022, **169**, 050531.
8 F. Walther, R. Koerver, T. Fuchs, S. Ohno, J. Sann, M. Rohnke, W. G. Zeier and J. Janek, *Chem. Mater.*, 2019, **31**, 3745–3755.
9 Y. Che, X. Hu, X. Lin, J. Guo and R. Teodorescu, *Energy Environ. Sci.*, 2023, **16**, 338–371.
10 W. Diao, S. Saxena and M. Pecht, *J. Power Sources*, 2019, **435**, 226830.
11 D. Huo, G. Li, G. Fan, X. Zhang, J. Han, Y. Wang, B. Zhou, S. Chen and L. Jia, *J. Power Sources*, 2025, **627**, 235830.
12 M. Schulze, M. T. F. Rodrigues, J. McBrayer, I. Bloom, A. Colclasure, G. Veith, A. Daniel, N. Neale, A. Burrell, J. Vaughey and C. Johnson, *Silicon Consortium Project Calendar Aging Electrochemical Screening Protocol 1.2*, **https://www.nrel.gov/transportation/silicon-anode-consortium.html**, (accessed September 2024).
13 J. Hartel, A. Banik, M. Y. Ali, B. Helm, K. Strotmann, V. Faka, O. Maus, C. Li, H. Wiggers and W. G. Zeier, *Chem. Mater.*, 2024, **36**, 10731–10745.
14 L. M. Riegger, S. Mittelsdorf, T. Fuchs, R. Rueß, F. H. Richter and J. Janek, *Chem. Mater.*, 2023, **35**, 5091–5099.
15 T. Zuo, F. Walther, J. H. Teo, R. Rueß, Y. Wang, M. Rohnke, D. Schröder, L. F. Nazar and J. Janek, *Angew. Chem., Int. Ed.*, 2023, **62**, e202213228.
16 R. Yang, Y. Xie, K. Li, W. Li, X. Hu, Y. Fan and Y. Zhang, *Appl. Therm. Eng.*, 2024, **252**, 123575.
17 Y. Li, Y. Cho, J. Cai, C. Kim, X. Zheng, W. Wu, A. L. Musgrove, Y. Su, R. L. Sacci, Z. Chen, J. Nanda and G. Yang, *Mater. Horiz.*, 2025, **12**, 119–130.
18 D. H. S. Tan, E. A. Wu, H. Nguyen, Z. Chen, M. A. T. Marple, J.-M. Doux, X. Wang, H. Yang, A. Banerjee and Y. S. Meng, *ACS Energy Lett.*, 2019, **4**, 2418–2427.
19 K. Kalaga, M.-T. F. Rodrigues, S. E. Trask, I. A. Shkrob and D. P. Abraham, *Electrochim. Acta*, 2018, **280**, 221–228.
20 F. Schomburg, B. Heidrich, S. Wennemar, R. Drees, T. Roth, M. Kurrat, H. Heimes, A. Jossen, M. Winter, J. Y. Cheong and F. Röder, *Energy Environ. Sci.*, 2024, **17**, 2686–2733.
21 A. Weng, E. Olide, I. Kovalchuk, J. B. Siegel and A. Stefanopoulou, *J. Electrochem. Soc.*, 2023, **170**, 090523.
22 J. Kim, W. Lee, J. Seok, S. Park, J. K. Yoon, S.-B. Yoon and W.-S. Yoon, *Cell Rep. Phys. Sci.*, 2023, **4**, 101331.
23 J. Zhu, M. S. Dewi Darma, M. Knapp, D. R. Sørensen, M. Heere, Q. Fang, X. Wang, H. Dai, L. Mereacre, A. Senyshyn, X. Wei and H. Ehrenberg, *J. Power Sources*, 2020, **448**, 227575.
24 A. Van der Ven, K. A. See and L. Pilon, *Battery Energy*, 2022, **1**, 20210017.
25 W. Zhang, F. H. Richter, S. P. Culver, T. Leichtweiss, J. G. Lozano, C. Dietrich, P. G. Bruce, W. G. Zeier and J. Janek, *ACS Appl. Mater. Interfaces*, 2018, **10**, 22226–22236.
26 Y. Zhu, X. He and Y. Mo, *ACS Appl. Mater. Interfaces*, 2015, **7**, 23685–23693.

27 R. Koerver, I. Aygün, T. Leichtweiß, C. Dietrich, W. Zhang, J. O. Binder, P. Hartmann, W. G. Zeier and J. Janek, *Chem. Mater.*, 2017, **29**, 5574–5582.
28 S. Dierickx, A. Weber and E. Ivers-Tiffée, *Electrochim. Acta*, 2020, **355**, 136764.
29 J. D. Huang, C. Meisel, N. P. Sullivan, A. Zakutayev and R. O'Hayre, *Joule*, 2024, **8**, 2049–2072.
30 J. Huang, N. P. Sullivan, A. Zakutayev and R. O'Hayre, *Electrochim. Acta*, 2023, **443**, 141879.
31 Y. Lu, C.-Z. Zhao, J.-Q. Huang and Q. Zhang, *Joule*, 2022, **6**, 1172–1198.
32 G. Whang, J. Huang, P. N. L. Pham, M. A. Kraft and W. G. Zeier, *ACS Electrochem.*, 2024, **1**, 249–262.
33 C.-Y. Yu, J. Choi, J. Dunham, R. Ghahremani, K. Liu, P. Lindemann, Z. Garver, D. Barchiesi, R. Farahati and J.-H. Kim, *J. Power Sources*, 2024, **597**, 234116.
34 S. Hori, R. Kanno, X. Sun, S. Song, M. Hirayama, B. Hauck, M. Dippon, S. Dierickx and E. Ivers-Tiffée, *J. Power Sources*, 2023, **556**, 232450.
35 W. J. Jeong, C. Wang, S. G. Yoon, Y. Liu, T. Chen and M. T. McDowell, *ACS Energy Lett.*, 2024, **9**, 2554–2563.
36 B. S. Vishnugopi, K. G. Naik, H. Kawakami, N. Ikeda, Y. Mizuno, R. Iwamura, T. Kotaka, K. Aotani, Y. Tabuchi and P. P. Mukherjee, *Adv. Energy Mater.*, 2023, **13**, 2203671.
37 S. Wenzel, S. J. Sedlmaier, C. Dietrich, W. G. Zeier and J. Janek, *Solid State Ionics*, 2018, **318**, 102–112.

